Nanoscale Advances

ROYAL SOCIETY OF CHEMISTRY

PAPER

View Article Online
View Journal | View Issue

Cite this: *Nanoscale Adv.*, 2026, **8**, 2107

Fe_3O_4@SiO_2@taurine: a magnetically recoverable green nanocatalyst for efficient synthesis of pyrano[2,3-*d*]pyrimidine derivatives

Charul Paliwal,[a] Aanchal,[a] Dharmendra,[a] P. S. Ranawat,[a] K. L. Ameta[b] and Chetna Ameta *[a]

Received 23rd October 2025
Accepted 30th January 2026

DOI: 10.1039/d5na00992h

rsc.li/nanoscale-advances

The development of recyclable and eco-friendly catalysts for heterocyclic synthesis remains a central theme in sustainable chemistry. Here, we present a magnetically recoverable Fe_3O_4@SiO_2@taurine catalyst, prepared by sequential silica coating and taurine functionalization of Fe_3O_4 nanoparticles. Structural, morphological, and magnetic characteristics were established through FT-IR, XRD, TEM, SEM-EDS, TGA, BET and ZETA analyses. This catalytic system promotes a one-pot, three-component reaction of aromatic aldehydes, malononitrile, and barbituric or thiobarbituric acid in aqueous ethanol under reflux, affording pyrano[2,3-*d*]pyrimidine derivatives in high yields and short reaction times. Ease of magnetic recovery, operational simplicity, and stable activity over multiple cycles highlight its practical applicability. Collectively, these findings demonstrate Fe_3O_4@SiO_2@taurine as a green, efficient, and recyclable platform for sustainable organic transformations.

1 Introduction

Catalyzed transformations, designed as efficient, green, and sustainable protocols, have been extensively explored in both academic laboratories and the chemical industry.[1] A major goal in catalysis is the development of systems with high activity, complete selectivity, low energy consumption, and long lifetime.[2] Performance is dictated by parameters such as size, morphology, electron distribution, surface composition, and stability.[3] With the advent of nanotechnology, nanocatalysts have demonstrated remarkable properties and are increasingly integrated into industrial processes.[4,5] Their role is especially important in nanochemistry and green chemistry, where the emphasis is on safe, energy-efficient reactions with minimal waste.[6,7] Heterogeneous nanocatalysts, in particular, offer high activity, simple recovery, and excellent recyclability, making them a valuable option for organic synthesis.[8–10] The design and synthesis of nanocatalysts through environmentally benign approaches has become a key driving force in heterogeneous catalysis and green chemistry.[11] The construction of heterocyclic scaffolds through multicomponent reactions has received great attention because of high atom economy and operational simplicity.[12–15]

Among various nanosystems, magnetic microspheres and core–shell structures have received significant attention due to their magnetic responsivity, low cytotoxicity, good stability, and surface tunability.[16–19] Core–shell magnetic silica microspheres, in particular, are attractive for bioseparation, enzyme immobilization, and catalysis.[20–22] Chemical co-precipitation offers a low-temperature, cost-effective route to prepare well-dispersed Fe_3O_4 nanoparticles with controlled size.[23] Their performance can be further improved by surface coating techniques.[24] Recently, core–shell nanocomposites that integrate inorganic nanoparticles with metal–organic frameworks (MOFs) have emerged as multifunctional materials. NP@MOF hybrids show wide applications across medicine, environment, and energy.[25,26] Among various MOFs, Fe-based systems stand out as heterogeneous catalysts due to their high dispersibility, abundance of active sites, and structural stability arising from strong Fe^{3+} carboxylate interactions, combined with their low toxicity, redox activity, and cost-effectiveness.[27–29] In this context, we designed a magnetically recoverable Fe_3O_4@SiO_2@taurine nanocatalyst for the one-pot, three-component synthesis of pyrano[2,3-*d*]pyrimidine derivatives, as illustrated in Scheme 1.

Magnetite (Fe_3O_4) is a highly attractive material for catalyst design due to its superior magnetic properties, conductivity, and biocompatibility compared to other ferrite oxides.[30] However, its poor stability and dispersibility necessitate protective coatings.[31] Silica serves as an excellent shell, offering chemical stability, thermal resistance, and abundant –Si–OH groups for further modification, thereby improving dispersibility, oxidation resistance, and biocompatibility.[32–34] Taurine (2-aminoethanesulfonic acid), a naturally occurring β-amino sulfonic acid, acts as a green bio-organic catalyst and an effective bifunctional donor–acceptor in condensation

[a]*Department of Chemistry, M. L. Sukhadia University, Udaipur, Raj-313001, India. E-mail: chetnaameta@mlsu.ac.in; chetna.ameta@yahoo.com*

[b]*Department of Applied Chemistry, Central University of Gujarat, Vadodara, Gujarat-391107, India*

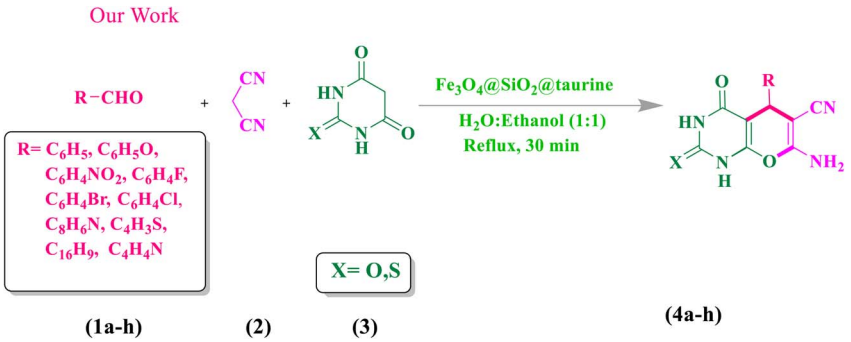

Scheme 1 Fe_3O_4@SiO_2@taurine-catalyzed preparation of pyranopyarimidines.

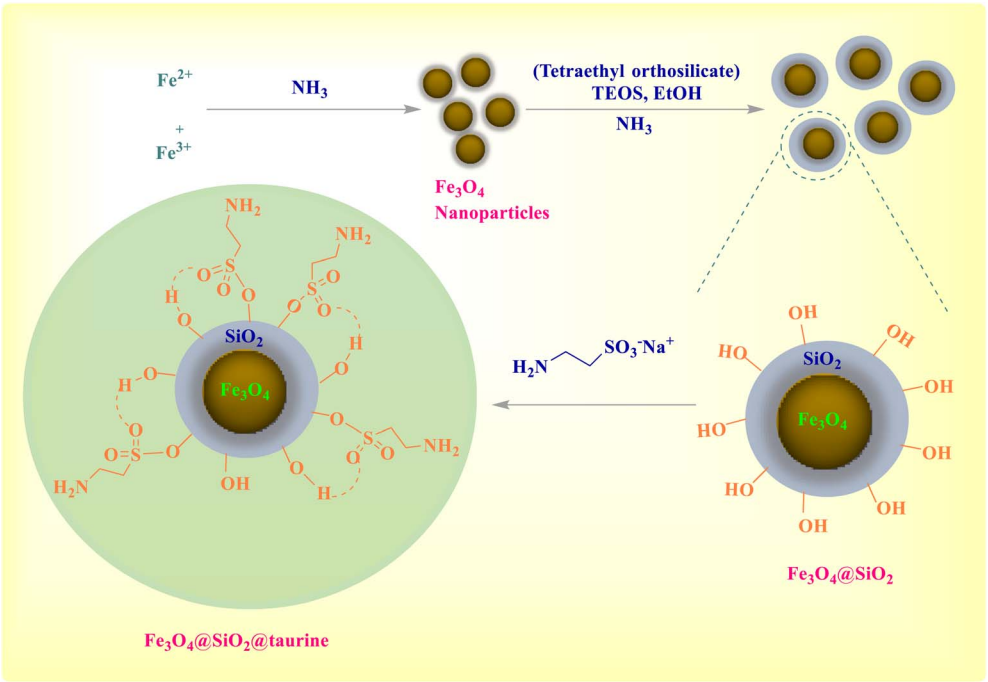

Scheme 2 Surface chemistry of the Fe_3O_4@SiO_2@taurine nanocatalyst.

reactions (Scheme 2).[35] It has been successfully employed for the synthesis of barbituric, thiobarbituric, and pyrano[2,3-*d*] pyrimidine derivatives under mild aqueous conditions, delivering high yields with advantages of low cost, non-toxicity, and reusability.[35,36] Considering the unique features of Fe_3O_4, the stabilizing role of silica, and the catalytic activity of taurine, Fe_3O_4@SiO_2@taurine was envisioned as a robust, magnetically recoverable nanocatalyst for one-pot, three-component syntheses of pyrano[2,3-*d*]pyrimidine derivatives under green conditions.

2 Experimental

2.1 Materials and methods

All reagents and chemicals used in the synthesis were procured from HiMedia, Sigma-Aldrich, and Alfa Aesar, and were used as received without further purification. Melting points of the synthesized compounds were determined using open capillary tubes on a Gallen Kamp apparatus and are uncorrected. The progress of reactions was monitored by thin-layer chromatography (TLC) using silica gel plates, with a mixture of ethyl acetate and *n*-hexane as the mobile phase. Fourier transform infrared (FT-IR) spectra were recorded using a PerkinElmer Spectrum RX-I FTIR spectrometer in ATR mode. Proton (^{1}H) and carbon (^{13}C) nuclear magnetic resonance (NMR) spectra were obtained using a Jeol 400 MHz spectrometer with deuterated dimethyl sulfoxide (DMSO-d_6) as the solvent. Elemental compositions were determined using an ELEMENTAR Vario EL III analyzer. Powder X-ray diffraction (XRD) patterns were recorded on a Panalytical X Pert Pro diffractometer. High-resolution transmission electron microscopy (HR-TEM) images were acquired using a Tecnai G2 20 S-TWIN [FEI] operated at 200 kV. Field emission scanning electron microscopy (FE-SEM) and energy-dispersive X-ray spectroscopy (EDX) analyses were conducted on a Nova Nano FE-SEM 450 (FEI). Thermogravimetric analysis (TGA) was carried out using

a EXSTAR TG/DTA 7300 at Central University of Gujarat. BET analysis was performed by using an Autosorb IQ-XR-XR-XR (3 Stat.) Viton and Zeta potential was measured by using a LITE-SIZER 500.

2.2 Synthesis of Fe_3O_4@SiO_2@taurine

2.2.1 Synthesis of Fe_3O_4 nanoparticles. A 500 mL solution of 1.5 M NaOH was first prepared and reserved. In a separate step, $FeCl_3 \cdot 6H_2O$ and $FeSO_4 \cdot 7H_2O$ were dissolved in 50 mL of 0.5 M HCl. The NaOH solution was then added dropwise to the iron salt solution under continuous stirring at 80 °C, leading to the formation of a black Fe_3O_4 precipitate. The product was magnetically separated, repeatedly washed with deionized water to remove residual ions, and dried at 50 °C.

2.2.2 Synthesis of silica-coated Fe_3O_4 nanoparticles (Fe_3O_4@SiO_2 NPs). To prepare silica-coated Fe_3O_4 nanoparticles (Fe_3O_4@SiO_2), 0.5 g of pre-synthesized Fe_3O_4 was dispersed in a mixture of 10 mL of deionized water, 30 mL of absolute ethanol, and 1 mL of 30% aqueous ammonia. The suspension was ultrasonicated in a water bath for 30 min to achieve uniform dispersion, followed by the dropwise addition of 2.5 mL tetraethyl orthosilicate (TEOS) under continuous stirring. The reaction mixture was stirred for 22 h at room temperature, after which the resulting Fe_3O_4@SiO_2 nanoparticles were magnetically separated and dried under ambient conditions.

2.2.3 Synthesis of silica-coated Fe_3O_4 functionalized with taurine (Fe_3O_4@SiO_2@taurine). In a 100 mL round-bottom flask, 3.5 g of taurine (2-aminoethanesulfonic acid) was dissolved in 40 mL of ethanol, followed by the addition of 3.5 g of Fe_3O_4@SiO_2 nanoparticles. The mixture was refluxed with constant stirring for 15 h, then cooled to room temperature,

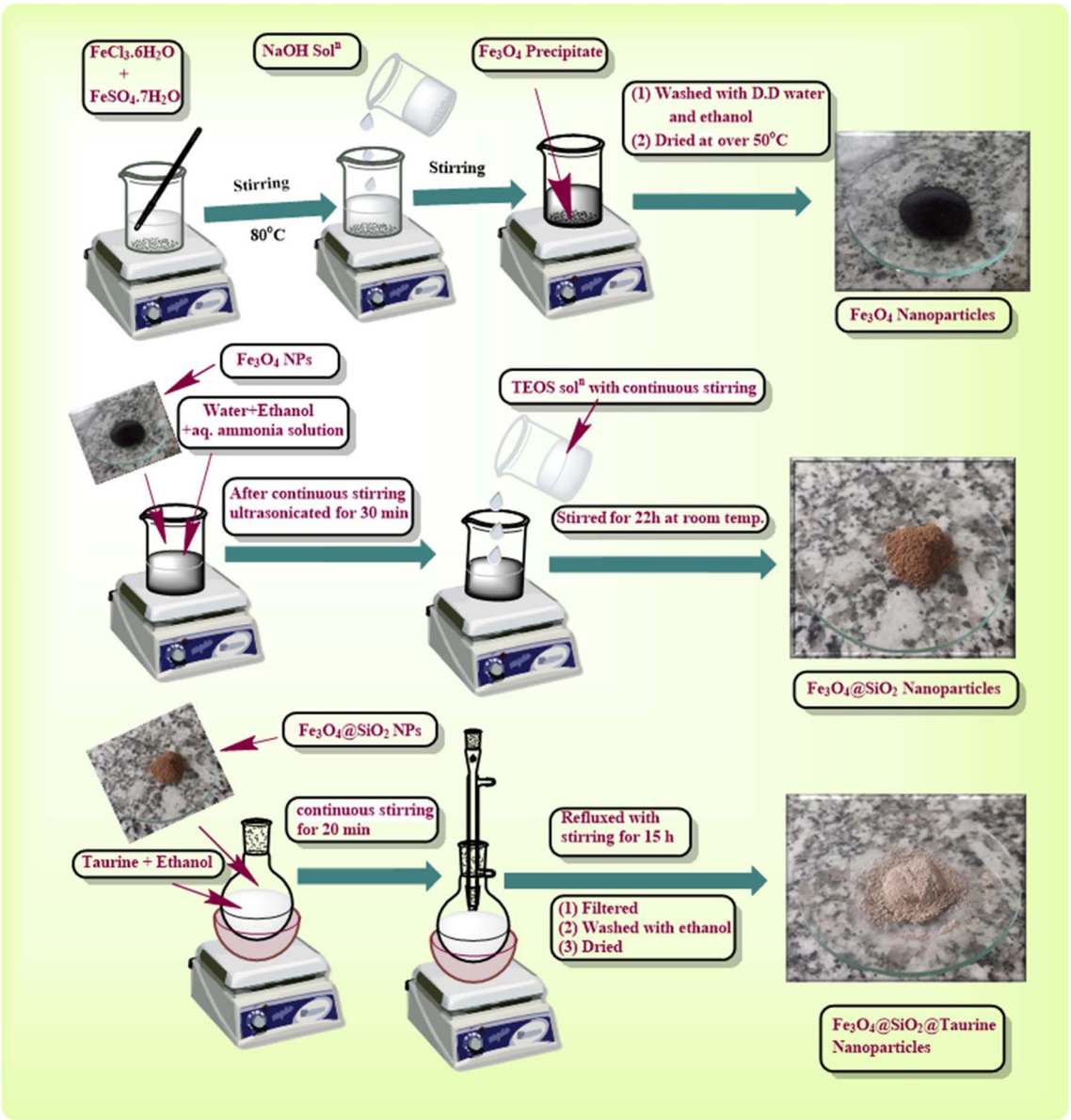

Fig. 1 The process of Fe_3O_4@SiO_2@taurine nanoparticle synthesis.

filtered, and thoroughly washed with ethanol to remove unreacted taurine. The obtained solid was dried under ambient conditions to afford the taurine-functionalized Fe_3O_4@SiO_2 catalyst (Fig. 1).

2.3 Framework for the synthesis of pyrano[2,3-*d*]pyrimidine derivatives

In a round-bottom flask, 1 mmol of an aromatic aldehyde, 1 mmol of malononitrile, 0.05 g of the catalyst, and a solvent mixture of ethanol and water (15 mL each) were combined and stirred at room temperature for 15 min. Subsequently, 1 mmol of barbituric acid or 2-thiobarbituric acid was added, and the reaction mixture was refluxed for 30 min. After completion, the mixture was cooled to room temperature, and the catalyst was separated using an external magnet. The crude product was filtered, washed with water, and recrystallized from ethanol to afford the pure pyrano[2,3-*d*]pyrimidines, which were finally dried in an oven at 60 °C.

2.3.1 Characterization

*2.3.1.1 7-Amino-2,4-dioxo-5-phenyl-1,3,4,5-tetrahydro-2H-pyrano[2,3-d]pyrimidine-6-carbonitrile (**4a**).* Mp. (°C): 205–206; yield: 97%; IR (ν_{max} cm^{-1}): 674 (C–H), 1093 (C–O–C str) 1183.58 (C–NH_2 str), 1445.19 (=CH str), 1587.20 (C=C str Ar), 1633 (C=C alkene str), 1712.28 (C=O str), 2191.50 (C≡N str), 2831.29 (C–H str), 3063.36 (=CH str), 3178.72 (NH_2 str) cm^{-1}. ^{1}H NMR (400 MHz, DMSO-d_6)/δ (ppm): 4.17 (s, 1H, C–H), 7.08 (2H, NH_2, D_2O exchangeable), 7.14–7.25 (m, 3H, Ar–H), 7.56–7.60 (t, J = 7.1, 2H, Ar–H), 11.04 (1H, NH, D_2O exchangeable). ^{13}C NMR (125 MHz, DMSO-d_6)/δ ppm: 39.3, 82.1, 113.8, 114.7, 130, 131, 131.8, 134.9, 162.

*2.3.1.2 7-Amino-5-(2-hydroxyphenyl)-2,4-dioxo-1,3,4,5-tetrahydro-2-H-pyrano[2,3-d]pyrimidine-6-carbonitrile (**4b**).* Mp. (°C):167–169; yield: 90%; IR (ν_{max} cm^{-1}): 1354.75 (C=C aromatic str), 1599.68, 1671.81 (C=O str), 2207.85 (C≡N str), 2311.98 (C–H), 3043.37 (NH), 3284.21 (NH_2), 3613.75 (OH), ^{1}H NMR (400 MHz, DMSO-d_6)/δ (ppm): 3.35 (s, 1H, H-5), 7.06 (d, 1H) 7.18 (2H, NH_2), 7.35 (d, J = 8, 1H) 7.67 (d, J = 8, 2H, H–Ar), 8.07 (d, J = 10.6, 2H, H–Ar), 10.98 (1H, NH). ^{13}C NMR (125 MHz, DMSO-d_6)/δ (ppm): 39.4, 78.9, 103, 114.9, 117.1, 125.8, 130.3, 135.7, 153.9, 154.4, 157.2.

*2.3.1.3 7-Amino-5-(4-nitrophenyl)-2,4-dioxo-1,3,4,5-tetrahydro-2-H-pyrano[2,3-d]pyrimidine-6-carbonitrile (**4c**).* Mp. (°C): 234–235; yield: 92%; IR (ν_{max} cm^{-1}): 821.08 (C–H), 975.02 (C–NO_2 str), 1180.71 (C–O–C str), 1273.78 (C–NH_2 str), 1340.95, 1516.81 (N=O str), 1403.38, 1516.81 (C=C str Ar), 1628.48 (C=C alkene str), 1713 (C=O str), 2188.60 (C≡N str), 2828.70 (C–H str), 3015.65 (=CH str), 3173.26 (NH_2 str). ^{1}H NMR (400 MHz, DMSO-d_6)/δ (ppm): 4.38 (s, 1H, C–H), 7.25 (2H, NH_2, D_2O exchangeable), 7.49 (dt, 2.5 Hz, 2H, Ar–H), 8.12 (dt, 2H, Ar–H), 11.11 (1H, NH, D_2O exchangeable), 12.16 (1H, NH, D_2O exchangeable). ^{13}C NMR (125 MHz, DMSO-d_6)/δ (ppm): 39.4, 58.4, 87.6, 124.5, 128.4, 146.1, 149.5, 153.4, 163.

*2.3.1.4 7-Amino-5-(4-fluorophenyl)-2,4-dioxo-1,3,4,5-tetrahydro-2H-pyrano[2,3-d]pyrimidine-6-carbonitrile (**4d**).* Mp. (°C): 264–265; yield: 93% IR (ν_{max} cm^{-1}): 837.95 (C–H), 1090.70 (C–O–C str), 1156.76 (C–F str), 1184.16 (C–NH_2 str), 1506.09, 1592.94 (C=C str Ar), 1632.90 (C=C alkene str), 1675.01, 1712.53 (C=O str), 2190.59 (C≡N str), 2828.35 (C–H str), 3000.92 (=CH str), 3175.77 (NH_2 str), 3382.83 (N–H str). ^{1}H NMR (400 MHz, DMSO-d_6)/δ (ppm): 4.20 (s, 1H, C–H), 6.88 (q, J = 8, 4H, Ar–H), 7.12–7.23 (m, 2H, NH_2, D_2O exchangeable), 11.0 (1H, NH, D_2O exchangeable). ^{13}C NMR (125 MHz, DMSO-d_6)/δ (ppm): 39.4, 59.3, 89, 113.1, 114.1, 117, 128, 128, 133.8, 133.9, 140, 150, 158.1, 160.1, 162.9.

*2.3.1.5 7-Amino-5-(3-bromophenyl)-2,4-dioxo-1,3,4,5-tetrahydro-2H-pyrano[2,3-d]pyrimidine-6-carbonitrile (**4e**).* Mp. (°C): 251–254; yield: 88% IR (ν_{max} cm^{-1}): 791.72, 879.03 (C–H), 1069.07 (C–Br str), 1103 (C–O–C str), 1204.64 (C–NH_2 str), 1470.16, 1527.18 (C=C aromatic str), 1658.22, 3090.93 (C=C alkene str), 1714.32 (C=O str), 2190.26 (C≡N str), 2937.96 (C–H str), 3001.83 (=CH str), 3313.26, 3409.93 (NH_2 str), 3735.60 (N–H str). ^{1}H NMR (400 MHz, DMSO-d_6)/δ (ppm): 4.23 (s, 1H, C–H), 7.14 (2H, NH_2, D_2O exchangeable), 7.19 (dt, 1H, Ar–H), 7.54 (t, J = 8, 1H, Ar–H), 7.90 (d, J = 1.8, 1H, Ar–H), 8.05 (t, J = 1.8, 1H, Ar–H), 11.04 (1H, NH, D_2O exchangeable), 12.05 (1H, NH, D_2O exchangeable). ^{13}C NMR (125 MHz, DMSO-d_6)/δ (ppm): 39.4, 58.7, 88.2, 114.3, 122, 127.1, 129.5, 132.1, 147.4, 150, 153, 158.2, 160.5.

*2.3.1.6 7-Amino-5-(2-chlorophenyl)-2,4-dioxo-1,3,4,5-tetrahydro-2H-pyrano[2,3-d]pyrimidine-6-carbonitrile (**4f**).* Mp. (°C): 210–212; yield: 89% IR (ν_{max} cm^{-1}): 749.59 (C–H), 1039.74 (C–Cl str), 1099.42 (C–O–C str), 1210.32 (C–NH_2 str), 1404.77, 1574.45 (C=C str Ar), 1617.82, 3038.65 (C=C alkene str) 1666.73, 1706.15 (C=O str), 2202.85 (C≡N str) 2820.95 (C–H str), 3038.65 (=CH str), 3314.60, 3167.96 (NH_2 str), 3519.40 (N–H str). ^{1}H NMR (400 MHz, DMSO-d_6)/δ (ppm): 4.68 (s, 1H, C–H), 7.13 (2H, NH_2, D_2O exchangeable), 7.18–7.20 (m, 1H, Ar–H), 7.23 (d, J = 4, Ar–H), 7.31 (d, J = 7.4, 1H, Ar–H), 11.04 (1H, NH, D_2O exchangeable), 12.08 (1H, NH, D_2O exchangeable). ^{13}C NMR (125 MHz, DMSO-d_6)/δ (ppm): 39.3, 86.9, 112.7, 114.1, 128.4, 130.1, 130.3, 130.9, 134.7, 135.4, 158.6.

*2.3.1.7 7-Amino-5-(3a,7a-dihydro-1H-indol-3-yl)-2,4-dioxo-1,34,5-tetrahydro-2H-pyrano[2,3-d]pyridine-6-carbonitrile (**4g**).* Mp.: > 300; yield: 91% IR (ν_{max} cm^{-1}): 1637.82 (C=C str), 2214.84 (C≡N str), 3016.85 (C–H Ar), 3272.36 (N–H), 3356.09 (N–H str). ^{1}H NMR (400 MHz, DMSO-d_6)/δ (ppm): 3.35 (s, 1H, H-5), 7.21 (2H, NH_2), 7.52 (d, J = 7.2, 2H, H–Ar), 8.0 (d, J = 7.2, 2H, H–Ar), 8.66 (d, J = 4.8,1H), 11.02 (1H, NH), 12.71 (1H, NH). ^{13}C NMR (125 MHz, DMSO-d_6)/δ (ppm): 39.3, 69.7, 119.5, 123.1, 127.3, 129.6, 133.9, 136.6, 140.3, 144.2, 150.9, 153, 163.8, 165.

*2.3.1.8 7-Amino-5-(4-nitrophenyl)-4-oxo-2-thioxo-1,3,4,5-tetrahydro-2H-pyrano[2,3-d]pyrimidine-6-carbonitrile (**4h**).* Mp.: 233–234 °C; yield: 90% IR (ν_{max} cm^{-1}): 694.85 (C–H), 817.17 (C–H), 962.56 (C–O str), 1120.03 (C–O–C str), 1239.78 (C=S str), 1350.14 (C–N str), 1404.22 (C–N str), 1472.59 (C=C str Ar), 1520.79 (N=O_2 symmetric str), 1565.46 (N=O_2 str Ar), 1683.26 (C=O str), 2198.83 (C≡N str), 2887.81 (C–H str), 3108.47 (C–H str Ar), 3185.25 (N–H str. symmetric), 3361.82 (N–H str asymmetric), ^{1}H NMR (400 MHz, DMSO-d_6)/δ (ppm): 4.45 (s, 1H, H-5), 6.13 (s, 2H, NH_2), 7.30 (d, J = 8, 2H, H–Ar), 8.14 (d, J = 8, 2H, H–Ar), 11.15 (s, 1H, NH), 12.50 (s, 1H, NH). ^{13}C NMR (125 MHz, DMSO-d_6)/δ (ppm): 35.8, 57.7, 92.9, 119.3, 124.1, 129.6, 147.1, 151.4, 152.4, 157.9, 161, 174.5.

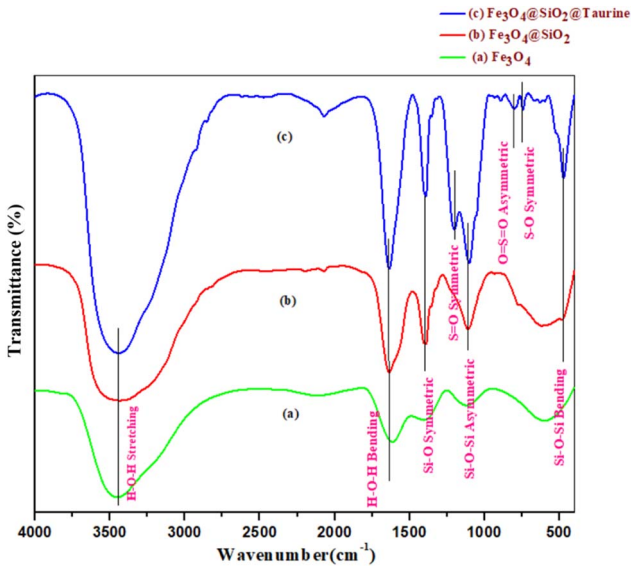

Fig. 2 FT-IR spectra of (a) Fe_3O_4, (b) Fe_3O_4@SiO_2, and (c) Fe_3O_4@SiO_2@taurine.

*2.3.1.9 7-Amino-5-(thiophen-2-yl)-4-oxo-2-thioxo-1,3,4,5-tetrahydro-2H-pyrano[2,3-d]pyrimidine-6-carbonitrile (**4i**).* Mp.: 280–284 °C; yield: 85% IR (ν_{max} cm^{-1}): 627.41 (C–S str), 734.38 (C–H str), 1138.57 (C–O str), 1217 (C–O–C str), 1259.13 (C=S str), 1302, 1398.83 (C–NH_2 str), 1518.46 (C=C str Ar), 1675.81 (C=O str), 2311.94 (C≡N str), 2883.24 (C–H str), 2996.53 (=CH str), 3110.25 (C–H str Ar), 3392.53 (NH_2 str). ^{1}H NMR (500 MHz, DMSO-d_6)/δ (ppm): 3.38 (s, 1H), 7.39 (d, J = 4.4, 1H, H–Ar), 8.25 (d, J = 1.89, 1H, H–Ar), 8.22 (d, J = 4.86, 1H), 12.42 (brs, 2H, NH). ^{13}C NMR (125 MHz, DMSO-d_6)/δ (ppm): 39.4, 112.2, 129.2, 137.4, 143.7, 146.9, 161.3, 162.2, 178.7.

*2.3.1.10 7-Amino-4-oxo-5-(pyren-2-yl)-2-thioxo-1,3,4,5-tetrahydro-2H-pyrano[2,3-d]pyrimidine-6-carbonitrile (**4j**).* Mp.: 250–252 °C; yield: 80% IR (ν_{max} cm^{-1}): 785.04 (C–H str), 944.44 (C–O str), 1054.71 (C–O–C str), 1226.28 (C=S str), 1326.62, 1388.25 (C–NH_2 str), 1517.14 (C=C str Ar), 1545.37 (N–H bending), 1675.25 (C=O str), 2312.16 (C≡N str), 2886.40 (C–H str Ar), 3392.76 (NH_2 str). ^{1}H NMR (500 MHz, DMSO-d_6)/δ (ppm): 3.39 (s, 1H), 8.23 (m, 2H), 8.42 (m, 4H), 8.63 (m, 3H), 9.14 (s, 1H, NH), 12.42 (brs, 2H, NH). ^{13}C NMR (125 MHz, DMSO-d_6)/δ (ppm): 39.9, 121.5, 133.4, 153.6, 159.6, 162, 179.5.

*2.3.1.11 7-Amino-5-(pyrrole-2-yl)-4-oxo-2-thioxo-1,3,4,5-tetrahydro-2H-pyrano[2,3-d]pyrimidine-6-carbonitrile (**4k**).* Mp.: 280–283 °C; yield: 85% IR (ν_{max} cm^{-1}): 745.66 (C–H str), 1147.88 (C–O str), 1179.41 (C–O–C str), 1224.37 (C=S str), 1315.68, 1381.39 (C–NH_2 str), 1510.59 (C=C str Ar), 1584.70 (N–H bending) 1655.07 (C=O str), 2220.82 (C≡N str), 2883.89 (C–H str), 3067.04 (C–H str Ar). ^{1}H NMR (500 MHz, DMSO-d_6)/δ (ppm): 3.38 (s, 1H), 6.59 (s, 2H, C–H), 7.43 (br, s, 2H, NH_2), 7.74 (s, 1H, C–H), 8.14 (s, 1H), 12.3 (s, 1H, NH), 13.3 (s, br, NH). ^{13}C NMR (125 MHz, DMSO-d_6)/δ (ppm): 106.7, 115.2, 129.7, 134.8, 141.3, 162.9, 178.1.

3 Results and discussion

3.1 Characterization of Fe_3O_4@SiO_2@taurine

3.1.1 Fourier transform infrared study. Fourier transform infrared (FT-IR) spectroscopy was used to analyze the functional groups and vibrational modes of (a) Fe_3O_4, (b) Fe_3O_4@SiO_2, and (c) Fe_3O_4@SiO_2@taurine, as illustrated in Fig. 2(a)–(c).

In curve (a), the FT-IR spectrum of Fe_3O_4 shows characteristic absorption bands at 618.41, 1632.15, and 3443.08 cm^{-1}, confirming the formation of iron oxide nanoparticles. The band at 618 cm^{-1} corresponds to Fe–O stretching vibrations, while

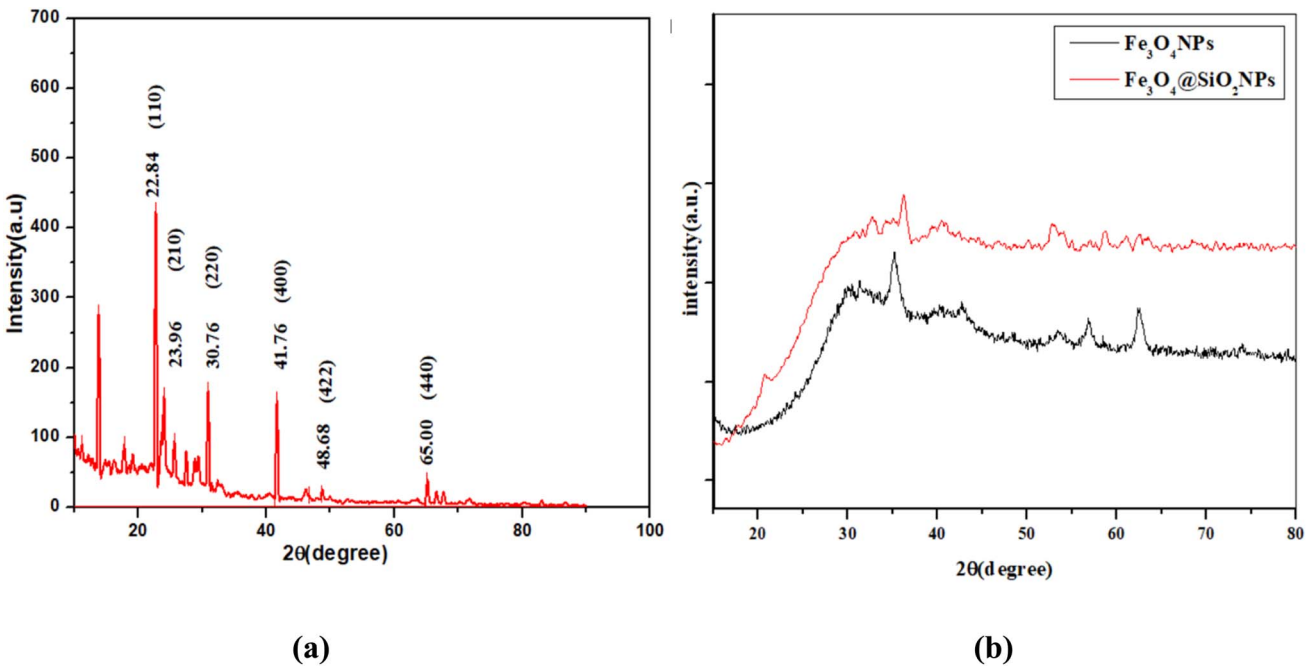

Fig. 3 X-ray diffraction (XRD) patterns of (a) the Fe_3O_4@SiO_2@taurine nanocomposite and (b) Fe_3O_4 and Fe_3O_4@SiO_2.

the peaks at 1632 and 3443 cm^{-1} are assigned to the bending and stretching vibrations of adsorbed water molecules (H–O–H), respectively.[37,38] In curve (b), corresponding to Fe_3O_4@SiO_2, additional absorption bands appear at 469.76, 616.11, 1108.49, 1389.05, 1634.64, and 3435.23 cm^{-1}, confirming successful silica coating. The strong band at 1108 cm^{-1} is assigned to Si–O–Si asymmetric stretching, while the peak near 1389.05 cm^{-1} corresponds to Si–O symmetric stretching. Furthermore, the band at 469.76 cm^{-1} is attributed to Si–O–Si bending vibrations, providing further evidence of the silica shell.[37,39]

In curve (c), representing the taurine-functionalized Fe_3O_4@SiO_2 catalyst, distinct peaks are observed at 470.32, 629.27, 745.74, 801.78, 890.86, 1101.40, 1200.05, 1390.11, 1634.84, 2069.19, and 3438.20 cm^{-1}. The absorption at 1200 cm^{-1} corresponds to S=O symmetric stretching. The presence of a band at 745 cm^{-1} is related to the stretching vibration of S–O, while the symmetric and asymmetric stretching bands of O=S=O appear at 801 cm^{-1} and 890.86 cm^{-1}, respectively, indicating successful taurine immobilization. The band at 2069 cm^{-1} is attributed to ammonium ions within the structure.[39] The consistent presence of Fe–O, Si–O–Si, and O–H related bands across all spectra confirms the preservation of the core–shell framework and the effectiveness of sequential surface modification. Collectively, these spectral features validate the stepwise synthesis of Fe_3O_4, silica encapsulation, and taurine functionalization.[37,39]

3.1.2 X-ray powder diffraction analysis. The X-ray diffraction (XRD) pattern of Fe_3O_4@SiO_2 @taurine is shown in Fig. 3(a)

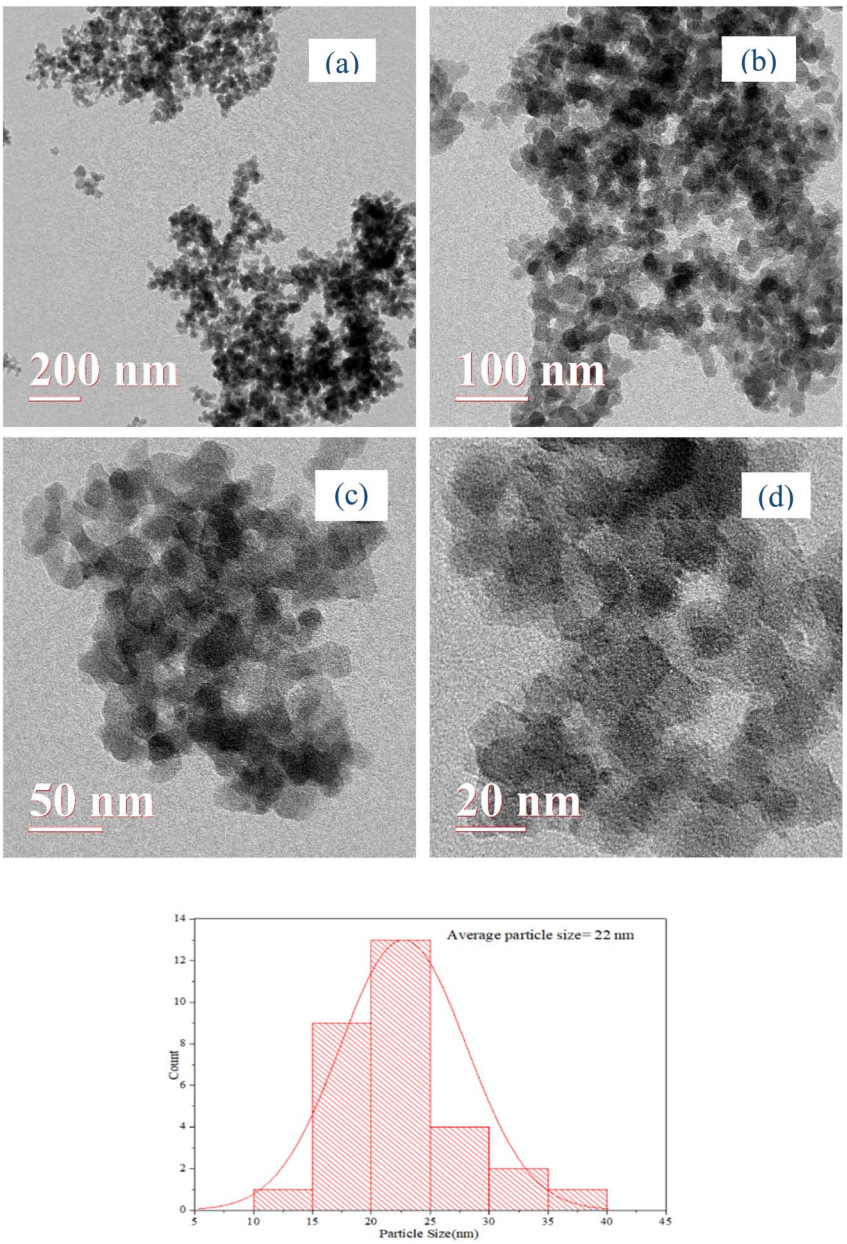

Fig. 4 (a)–(d) TEM images of Fe_3O_4@SiO_2@taurine.

and (b). Distinct diffraction peaks at $2\theta = 30.76°$, 41.76°, 48.68°, and 65.00° correspond to the (220), (400), (422), and (440) planes of the cubic inverse spinel structure of Fe_3O_4, confirming that the magnetic core preserved its crystallinity during surface modification (JCPDS 019-0629).[37] Additionally, a broad reflection centered at $2\theta = 22.84°$ with a full width at half maximum (FWHM) of 0.0087 was observed, which is characteristic of amorphous silica and indicates the presence of taurine-functionalized SiO_2.[40] The most intense peak at 22.84 was further used to estimate the average crystallite size of the nanoparticles. Overall, the XRD analysis confirms the successful formation of Fe_3O_4@SiO_2@taurine, with the Fe_3O_4 core retaining its spinel structure after silica coating and taurine functionalization.

The average crystallite size of the Fe_3O_4@SiO_2@taurine nanoparticles was estimated using the Scherrer equation:

$$D = K\lambda/\beta \cos$$

where D is the crystallite size, K is the shape factor (0.9), λ is the X-ray wavelength (0.15406 nm for Cu Kα radiation), β is the full width at half maximum (FWHM) of the diffraction peak (in radians), and θ is the Bragg angle. Using the (110) diffraction peak, the average crystallite size was determined to be ~16.6 nm, confirming the nanocrystalline nature of the Fe_3O_4@SiO_2@taurine composite.

3.1.3 Transmission electron microscopy (TEM). TEM was used to examine the morphology, particle size, and structural characteristics of the Fe_3O_4@SiO_2@taurine nanocomposite. To further analyze the particle dimensions, a particle size distribution histogram was constructed based on measurements of many particles. The histogram indicates a narrow size distribution with an average particle diameter of approximately 22 nm. The TEM images in Fig. 4(a)–(d) show that the nanoparticles possess a nearly spherical shape with a narrow size distribution, and the mean particle diameter was determined to be about 22 nm. The micrographs also display a distinct core–shell arrangement, verifying the successful fabrication of the Fe_3O_4@SiO_2@taurine nanostructure with well-dispersed spherical particles.

3.1.4 Scanning electron microscopy (SEM) and energy-dispersive X-ray spectroscopy (EDS). The Fe_3O_4@SiO_2@taurine nanocomposite was synthesized by coating magnetite (Fe_3O_4) with a silica layer subsequently functionalized with taurine. Scanning electron microscopy (SEM) was employed to examine the surface morphology, while energy-dispersive X-ray spectroscopy (EDS) was carried out to determine the elemental composition of the material. As illustrated in Fig. 5(a)–(d), the SEM micrograph demonstrates that the Fe_3O_4@SiO_2@taurine nanoparticles are predominantly spherical and exhibit a fairly uniform distribution. The mean particle size was calculated to be around 22 nm.

The EDS spectra in Fig. 6(a)–(i) verify the elemental composition of the Fe_3O_4@SiO_2@taurine nanocomposite. Clear signals for Fe, Si, and O correspond to the magnetite core and silica coating, while the additional peaks for sulfur (S) and nitrogen (N) originate exclusively from the sulfonic acid (–SO_3H) and amino (–NH_2) groups of taurine. The quantitative analysis revealed elemental proportions of approximately 0.2% Fe, 5.5% Si, 41.1% O, 1.2% S, 47.3% C, and 4.7% N. The detection of S and N peaks, which are absent in Fe_3O_4 and SiO_2, provides direct confirmation of taurine functionalization on the silica shell and validates the successful formation of the nanocomposite.

3.1.5 Thermogravimetric analysis (TGA). The thermal stability of Fe_3O_4@SiO_2@taurine nanoparticles was investigated by thermogravimetric analysis (TGA) over the temperature

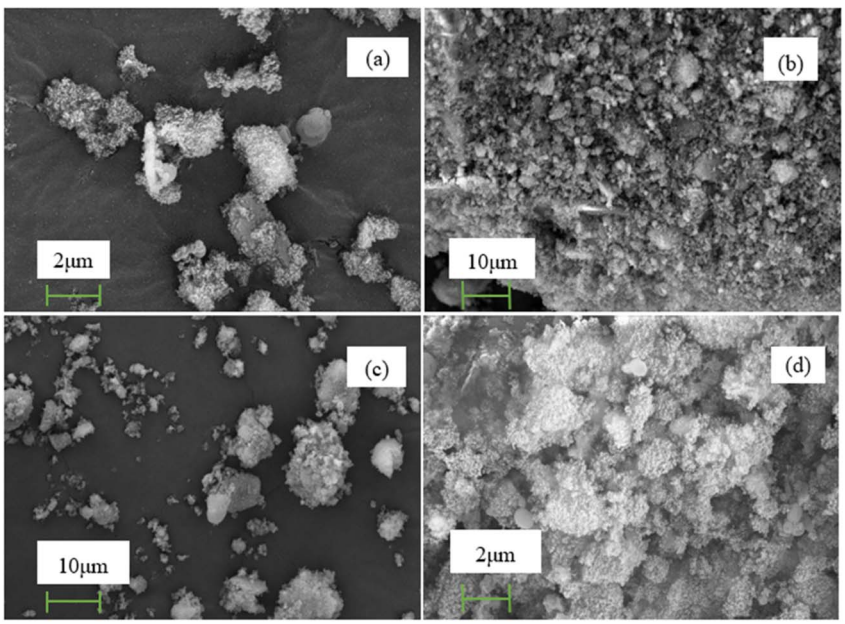

Fig. 5 (a)–(d) SEM images of Fe_3O_4@SiO_2@taurine nanoparticles.

range of 20–700 °C under air (Fig. 7). The TGA curve provides insight into the compositional stability and thermal decomposition behaviour of the nanocomposite. An initial weight loss between 50–250 °C is attributed to the removal of adsorbed moisture and dehydration of surface-bound water molecules. A subsequent weight loss observed between 300–600 °C corresponds to the decomposition of organic functional groups (–OH, $–SO_3H$, and $–NH_2$) attached to the nanocatalyst surface. These findings indicate that the Fe_3O_4@SiO_2@taurine nanocomposite exhibits good thermal stability, while the second decomposition stage confirms the successful surface functionalization with taurine-derived groups.

3.1.6 Zeta potential analysis. The Fe_3O_4@SiO_2@taurine catalyst exhibited a mean zeta potential of +3.5 ± 2.1 mV, indicating a near-neutral surface charge and limited electrostatic stabilization (Fig. 8). This is consistent with the zwitterionic nature of taurine functionalization, where protonated amine ($–NH^{3+}$) and sulfonate ($–SO^{3-}$) groups partially neutralize each other. The dispersion pH was measured to be 6.9, confirming that the surface functional groups are in their expected protonation state under reaction conditions. The relatively high conductivity of the suspension (1.85 mS cm^{-1}) and sample turbidity can further reduce the observed zeta potential (ζ).

Despite the low zeta potential, the catalyst demonstrates excellent heterogeneous catalytic activity, high yields, and easy magnetic recoverability, indicating that the active Fe sites and taurine groups remain accessible to the substrate during reactions. The near-neutral surface charge may also reduce undesired electrostatic interactions, enhancing substrate approach and facilitating recyclability. Overall, the measured zeta potential and pH confirm the chemical stability and practical applicability of Fe_3O_4@SiO_2@taurine as an efficient, magnetically separable heterogeneous nanocatalyst.

3.1.7 BET analysis. The textural properties of the synthesized catalyst were examined using N_2 adsorption–desorption analysis at 77 K (Fig. 9). The BET plot exhibited a linear region

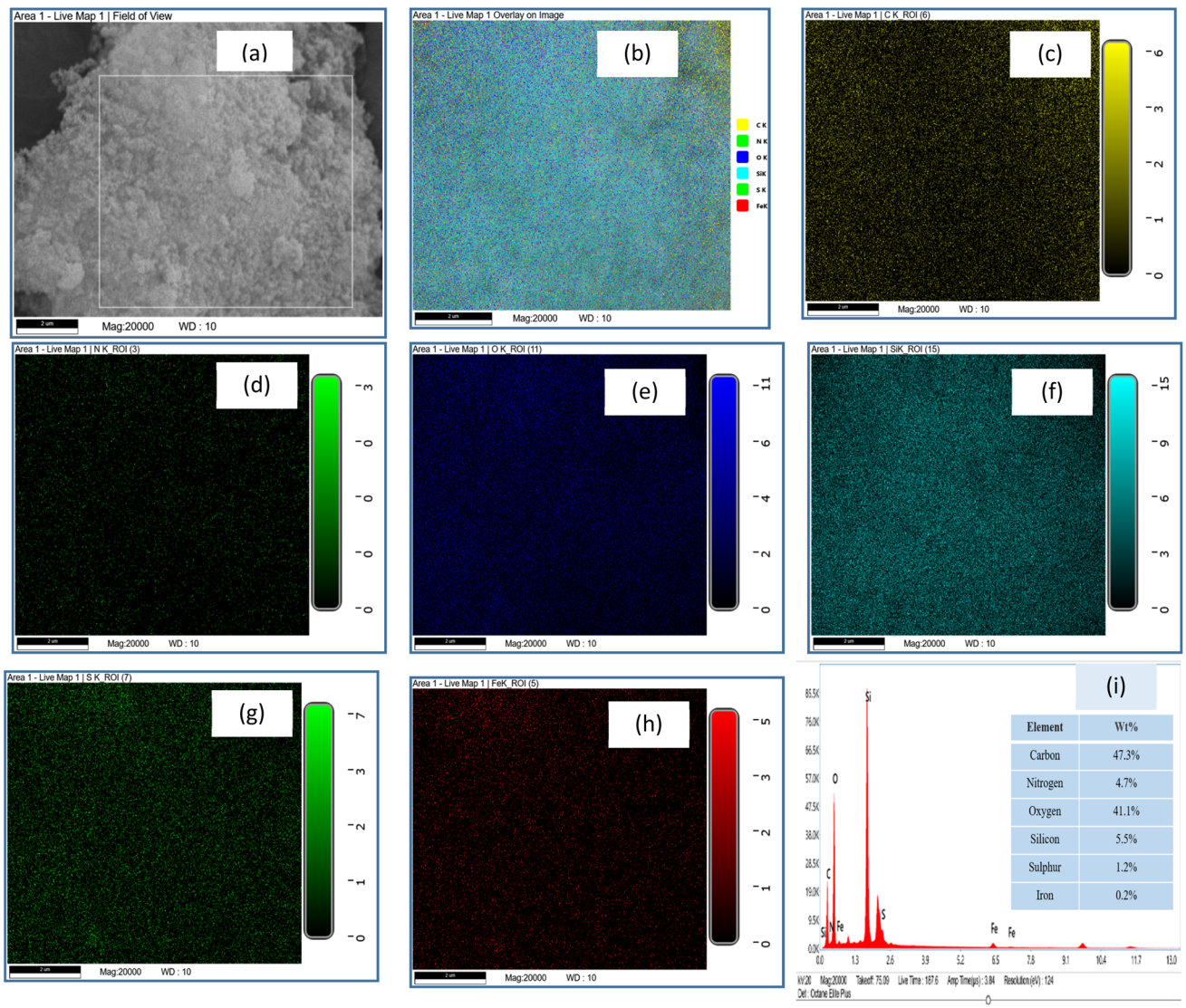

Fig. 6 (a)–(i) EDS spectrum showing the presence of Fe, Si, O, S, C, and N, confirming the encapsulation of Fe_3O_4 within the silica shell and its functionalization with taurine.

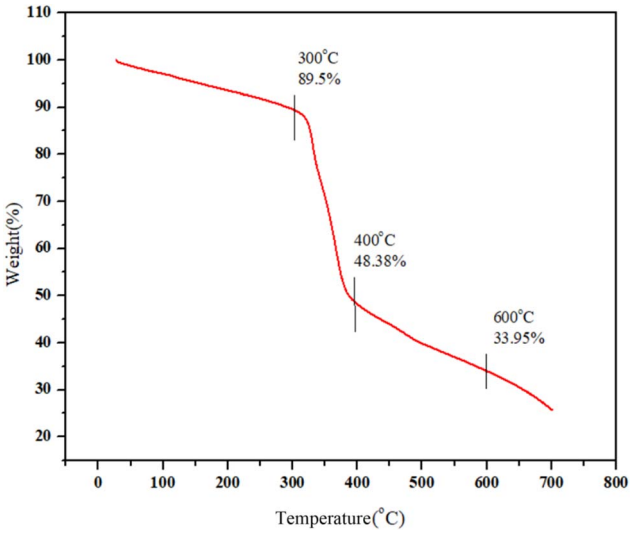

Fig. 7 TGA curve of Fe_3O_4@SiO_2@taurine nanoparticles.

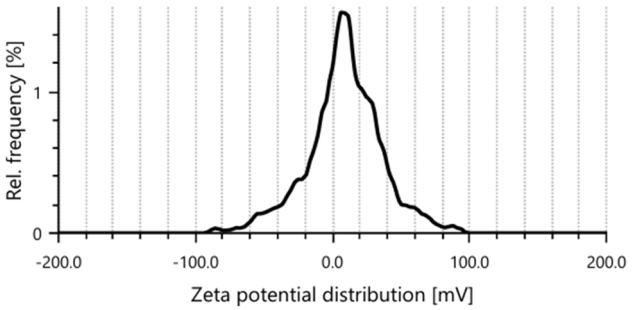

Fig. 8 Zeta potential of Fe_3O_4@SiO_2@taurine nanoparticles.

with a correlation coefficient of 0.9995, yielding a specific surface area of 4.203 m^2 g^{-1}. The surface area is consistent with dense iron oxide based catalysts and supports the observed catalytic activity, as the mesoporous architecture provides sufficient accessibility of active sites while maintaining structural stability. A moderate surface area prevents excessive adsorption of reactants and minimizes catalyst degradation or loss of active sites during repeated catalytic cycles.

The XRD and TEM/SEM analyses confirmed that the Fe_3O_4 core retains its crystalline inverse spinel structure after surface modification and that the Fe_3O_4@SiO_2@taurine nanocatalyst possesses a well-defined spherical core–shell morphology with an average particle size of ~22 nm. FT-IR spectroscopy and EDS analysis verified the successful immobilization of taurine on the silica surface through the appearance of characteristic sulfonic and amino functional groups, along with the presence of sulphur and nitrogen signals absent in the unmodified materials. TGA measurements demonstrated good thermal stability of the nanocomposite and further confirmed the presence of organic taurine moieties on the catalyst surface. In addition, zeta potential analysis revealed a near-neutral surface charge (+3.5 mV), consistent with the zwitterionic nature of taurine and indicative of chemical stability under reaction conditions. BET analysis showed a specific surface area of 4.203 m^2 g^{-1}, characteristic of iron oxide-based mesoporous materials, providing sufficient accessibility of active sites while maintaining structural robustness. Collectively, these results confirm the successful synthesis, surface functionalization, stability, and catalytic suitability of the Fe_3O_4@SiO_2@taurine nanocatalyst.

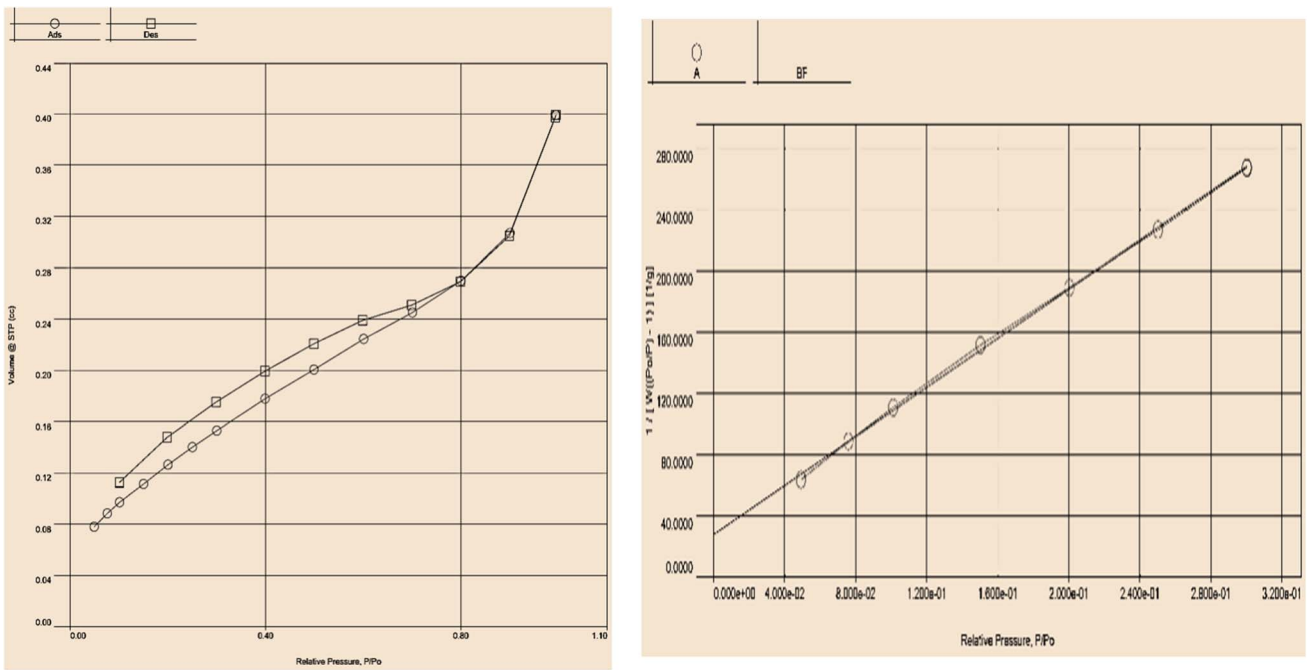

Fig. 9 BET analysis of Fe_3O_4@SiO_2@taurine nanoparticles.

Table 1 The model condensation reaction of aromatic aldehydes (1 mmol), malononitrile (1 mmol), and barbituric acid (1 mmol) under various conditions

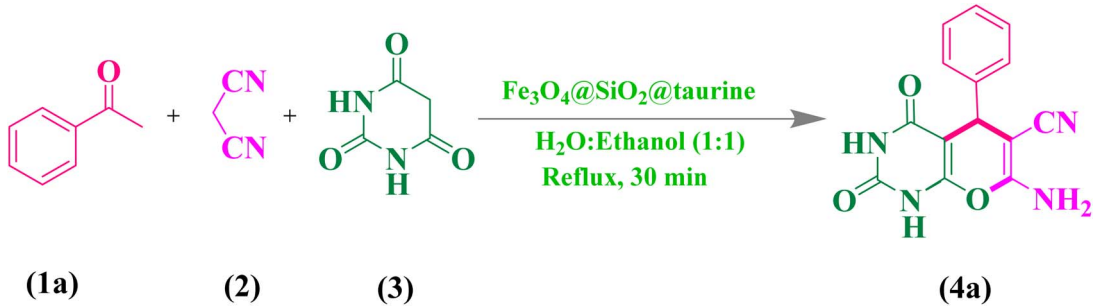

S. no.	Catalyst	Solvent	Time (min)	Condition	Yield%
1	Catalyst free	Solvent free	180	90 °C	NA
2	Catalyst free	H_2O	180	R.T.	NA
3	Fe_2O_3	H_2O	120	R.T.	65
4	SiO_2	EtOH	80	R.T.	55
5	Fe_3O_4 NPs	H_2O	60	70 °C	68
6	Fe_3O_4@SiO_2	H_2O : EtOH	60	Reflux	78
7	Fe_3O_4@SiO_2@taurine (0.005 g)	Solvent free	80	70 °C	50
8	Fe_3O_4@SiO_2@taurine (0.005 g)	Acetone	80	Reflux	60
9	Fe_3O_4@SiO_2@taurine (0.005 g)	H_2O : EtOH	80	Reflux	82
10	Fe_3O_4@SiO_2@taurine (0.01 g)	H_2O : EtOH	60	Reflux	84
11	Fe_3O_4@SiO_2@taurine (0.03 g)	H_2O : EtOH	45	Reflux	90
12	Fe_3O_4@SiO_2@taurine (0.05 g)	Solvent free	30	85 °C	85
13	Fe_3O_4@SiO_2@taurine (0.05 g)	H_2O : EtOH	30	Reflux	97

3.2 The study of catalytic activity of Fe_3O_4@SiO_2@taurine MNPs in the synthesis of pyrano[2,3-*d*]pyrimidines

To determine the optimum reaction conditions, a model three-component condensation reaction between an aromatic aldehyde, malononitrile, and barbituric acid was conducted using Fe_3O_4@SiO_2@taurine as a catalyst. The reaction was examined under different reaction conditions and reflux for yield comparison. Under reflux, the transformation was completed within 30 min, affording 97% of the target product (Table 1, entry 13), whereas no product formation occurred in water at room temperature without a catalyst and solvent (Table 1, entry 1). When the reaction proceeded in the absence of a catalyst in water for 180 min at room temperature, the desired product was not formed (Table 1, entry 2). Using Fe_3O_4 as a catalyst in water provided only 65% yield after 120 min at room temperature (Table 1, entry 3), while SiO_2 in ethanol gave 55% yield in 80 min at room temperature (Table 1, entry 4). Nano-Fe_2O_3 alone improved the yield to 68% in 60 min at 70 °C (Table 1, entry 5). The use of Fe_3O_4@SiO_2 in a mixed solvent system of H_2O : EtOH led to an enhanced yield of 78% under reflux in a shorter reaction time (Table 1, entry 6). Furthermore, we investigated

Table 2 Comparison of Fe_3O_4/SiO_2@taurine and various catalysts in the synthesis of pyrano[2,3-*d*]pyrimidine derivatives

S no.	Catalyst	Solvent	Condition	Time (min)	Yield	Year/Ref
1	Et_3N	DMF	MW	10–12	65–70	2003 (ref. 41)
2	DAHP	EtOH	R.T.	120	71–81	2008 (ref. 42)
3	L-Proline	Aq. EtOH	Reflux	30–120	68–85	2009 (ref. 43)
4	$[KAl(SO_4)_2]$	H_2O	80 °C	30–45	81–88	2010 (ref. 44)
5	α-Fe_2O_3	EtOH	R.T.	30	93	2011 (ref. 45)
6	Zn[(L)proline]2	EtOH	Reflux	30–720	80–90	2019 (ref. 46)
7	SBA-Pr-SO_3H	Solvent free	140 °C	5–45	91	2013 (ref. 47)
8	DMA	EtOH	Reflux	20	90	2014 (ref. 48)
9	$Zn[(L)proline]_2$	EtOH	Reflux	30–720	80–90	2019 (ref. 46)
10	γ-Fe_2O_3@SiO_2@[BisAPTES]Cl_2-NPs	H_2O : EtOH (2 : 1)	80 °C	12	85	2019 (ref. 49)
11	Nano-Fe_3O_4@APTES@isatin-SO_3H MNPs	EtOH : H_2O	Reflux	7–25	86–95	2019 (ref. 50)
12	β-CD	H_2O	80 °C	10	93	2020 (ref. 51)
13	$CoFe_2O_4$@FA-Er	H_2O	100 °C	15	96	2021 (ref. 52)
14	Fe_3O_4@SiO_2@taurine	H_2O : EtOH	Reflux	30	97	This work

Table 3 Catalyzed multi-component synthesis of pyrano[2,3-*d*]pyrimidine derivatives

S. no	Aldehyde	Barbituric/thiobarbituric acid	Product	Yield	Time (min)	TON/TOF (h^{-1})	M. P (observed/ reported)
1	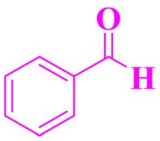 1a	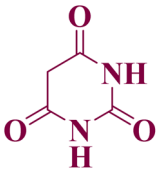	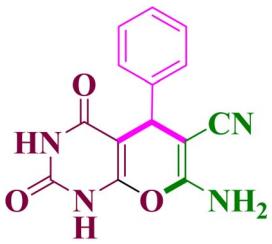 4a	97%	15	154.8/619	205–206/205–207
2	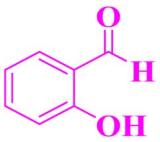 1b	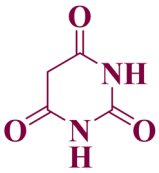	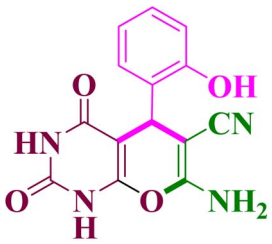 4b	90%	30	143.6/287.2	167–169/168–69
3	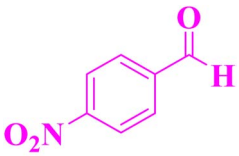 1c	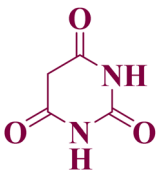	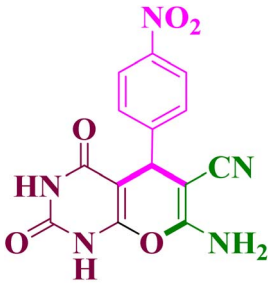 4c	92%	15	146.7/586.8	234–235/236–237
4	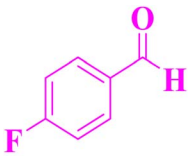 1d	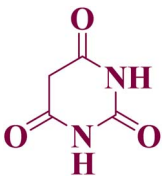	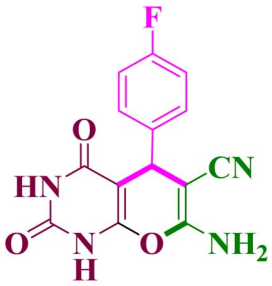 4d	93%	15	148.3/593.2	264–265/268–270
5		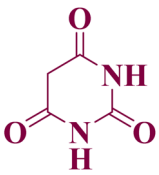		88%	15	140.4/561.4	251–254/254–255

Table 3 (*Contd.*)

S. no	Aldehyde	Barbituric/thiobarbituric acid	Product	Yield	Time (min)	TON/TOF (h^{-1})	M. P (observed/ reported)
	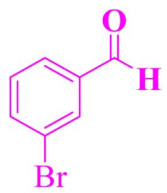 1e		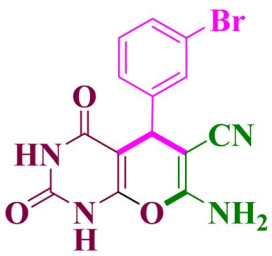 4e				
6	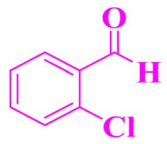 1f	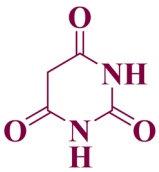	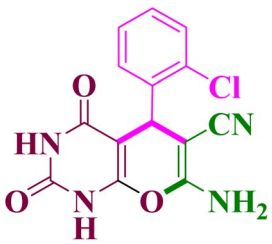 4f	89%	25	141/338.4	210–212/211–212
7	 1g	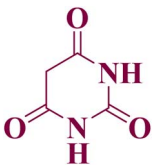	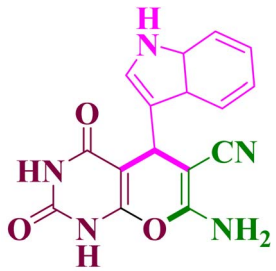 4g	91%	25	145.1/348.2	>300/>300
8	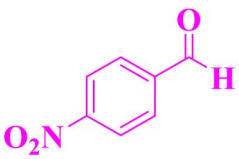 1h	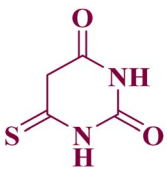	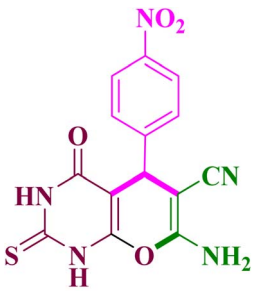 4h	90%	30	143.6/287.2	233–234/235–236
9	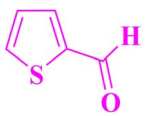 1i	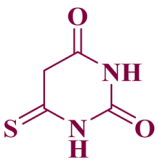	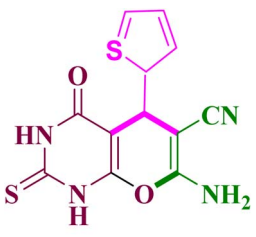 4i	85%	15	135.6/542.4	280–284/280–282

Table 3 (*Contd.*)

S. no	Aldehyde	Barbituric/thiobarbituric acid	Product	Yield	Time (min)	TON/TOF (h^{-1})	M. P (observed/ reported)
10	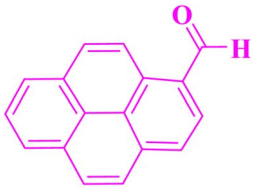 1j	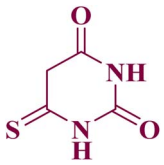	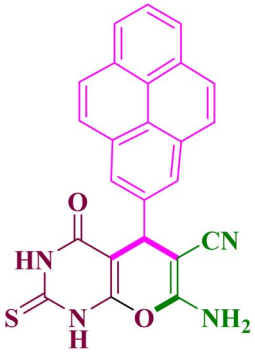 4j	80%	30	127.6/255.2	250–252
11	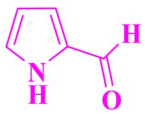 1k	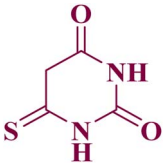	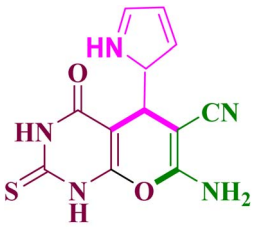 4k	85%	20	135.6/406.8	280–283/283–284

the solvent free condition effect on the sample reaction. When 0.005 g of Fe_3O_4@SiO_2@taurine was added in the reaction without solvent at 70 °C, the yield decreased to 50% (Table 1, entry 7). Catalyst loading studies showed that 0.005 g of catalyst resulted in 60% and 82% yield in 80 min in the presence of acetone and H_2O : EtOH, respectively (Table 1, entries 8 & 9). Increasing the catalyst loading from 0.01 to 0.05 g resulted in a marked improvement in yield from 84 to 97% with a concomitant reduction in reaction time (Table 1, entries 10–13); notably, the optimized catalyst amount also showed good efficiency under solvent-free conditions, affording an 85% yield at 85 °C within 30 min. Based on these results, the optimized condition was identified as refluxing benzaldehyde, malononitrile, and barbituric acid in H_2O : EtOH (1 : 1) using 0.05 g of Fe_3O_4@SiO_2@taurine (Table 1, entry 13). The use of ethanol, water, or their mixture as green solvents provides additional benefits, including environmental safety, non-toxicity, low cost, and operational simplicity.

Table 1 summarizes the effect of various catalysts, solvents, reaction times and conditions on the yield of a chemical reaction. Notably, after functionalization of the catalyst with taurine (entries 9–13), both efficiency and reaction speed were significantly boosted. As the taurine functionalized catalyst increased from 0.005 to 0.05 g, the yield steadily enhanced from 82 to 97%, while the reaction time decreased from 80 to 30 min. These results highlight the synergistic effect of taurine modified Fe_3O_4@SiO_2 in providing enhanced catalytic performance, likely due to increase surface activity and better interaction with the reactants under reflux in a polar protic solvent system. The 0.05 g loading represents an optimal balance of catalytic power and operational efficiency, making it the most effective condition for the synthesis of pyrano[2,3-*d*]pyrimidine derivatives.

Table 2 presents a comparative study of previously reported catalysts with Fe_3O_4@SiO_2@taurine. The data in the table clearly establish that the catalyst Fe_3O_4@SiO_2@taurine, synthesized in this work, performs comparatively better than previously reported catalysts in terms of yield and reaction time under mild conditions. It achieved an impressive 96% yield in just 30 minutes under reflux conditions in a green solvent system (H_2O : EtOH). Additionally, many other catalysts require longer reaction times or give lower yields. The synthesized Fe_3O_4@SiO_2@taurine catalyst combines high efficiency, short reaction time, excellent yield, a non-toxic, environmentally friendly and straightforward approach with simple workup and easy recovery, making it an efficient and practical catalyst for the synthesis of pyrano[2,3-*d*]pyrimidine derivatives.

The TON and TOF values in this study were calculated on the basis of the Fe wt% present in the catalyst, which is the accepted method for heterogeneous nanocatalysts where metal atoms serve as the true catalytic sites (Table 3). Similar metal loading-

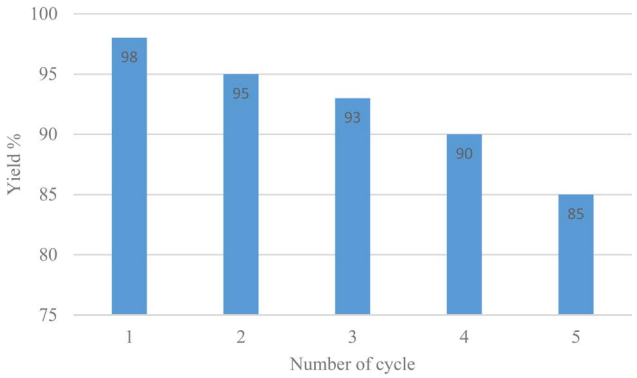

Fig. 10 Recyclability of Fe_3O_4@SiO_2@taurine.

based TON/TOF evaluation approaches have been reported for related magnetic and organometallic catalyst systems.[53–56]

3.3 Recyclability and reusability of Fe_3O_4@SiO_2@taurine

From the perspective of green and sustainable chemistry, evaluating the recyclability and reusability of the catalyst is crucial for both environmental and economic considerations. After each reaction cycle, the nanocatalyst was conveniently separated using an external magnet and washed with ethanol. Before reuse of the catalyst in the reaction, the catalyst was dried at 60 °C. The recyclability test over five consecutive runs showed that the catalyst retained nearly the same activity, affording yields in the range of 98–90% up to four cycles but the yield of compound **4a** was decreased with increase in reaction time in the fifth cycle (yield 85%) (Fig. 10). As shown in Fig. (11), the FTIR spectrum of recycled Fe_3O_4@SiO_2@taurine after the fourth run exhibited that the catalyst could be reused numerous times without significant loss in yield%, chemical stability and structure integrity of the catalyst. The catalyst retained 85% yield after five consecutive cycles, indicating moderate recyclability.

3.4 Mechanism of reaction

Mechanistic pathways involving base-mediated condensation and cyclization reactions have been described in several organic methodology studies.[57] The plausible mechanism for the Fe_3O_4@SiO_2@taurine-catalyzed synthesis of pyrano[2,3-*d*]pyrimidine derivatives is illustrated in Scheme 3. Initially, the nanocatalyst, acting as a bifunctional donor–acceptor, activates the carbonyl group of the aromatic aldehyde (**1**) to form intermediate (**1a**). Concurrently, malononitrile (**2**) undergoes a Michael addition with barbituric acid (**3**), followed by tautomerization to yield intermediates (**2a**) and (**3a**). A Knoevenagel condensation between (**2a**) and (**1a**) produces adduct (A), which undergoes a subsequent Michael addition with (**3a**) to form adduct (B). This intermediate tautomerizes (imine-enamine shift) to (C), undergoes cyclization to afford (D), and finally tautomerizes to furnish the desired pyrano[2,3-*d*]pyrimidine (A).

The substituent effects observed in the synthesis correlate strongly with the rate-determining step of the proposed mechanism. The reaction initiates with catalyst-assisted activation of the aldehyde through hydrogen bonding with the sulfonic acid group of taurine, followed by nucleophilic attack of the malononitrile anion generated at the basic NH_2/NH_3^+ sites. Aldehydes containing electron-withdrawing groups exhibit enhanced reactivity because their carbonyl carbons possess increased electrophilicity, facilitating rapid formation of the Knoevenagel intermediate. However, aldehydes containing electron-withdrawing substituents reacted faster with malononitrile and barbituric acid, affording the products in higher yields and shorter reaction times compared to those bearing electron-donating groups. The presence of electron-withdrawing substituents enhances the positive (electrophilic) character of the carbonyl carbon, thereby lowering the activation energy required for nucleophilic attack by the malononitrile-

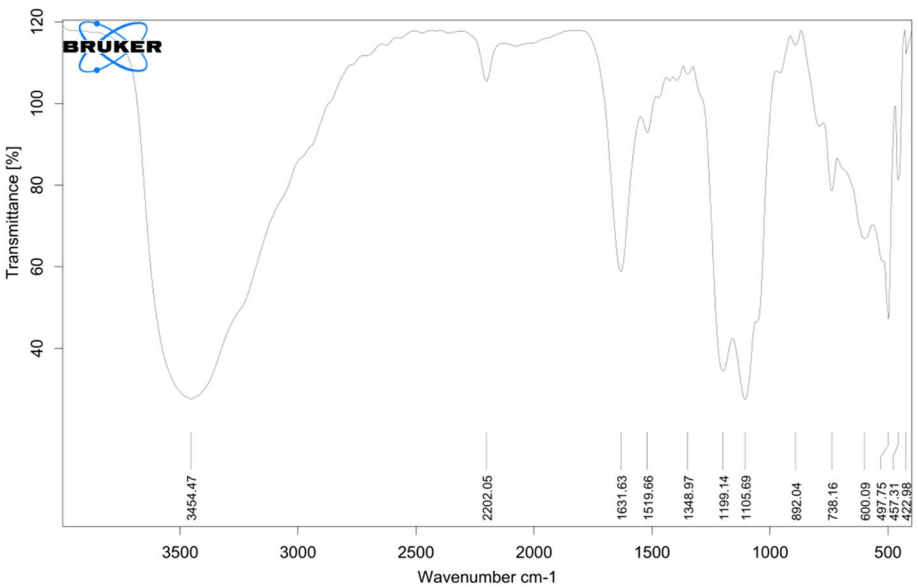

Fig. 11 FTIR spectrum of recovered Fe_3O_4@SiO_2@taurine nanoparticles after 4 reuses in the reaction.

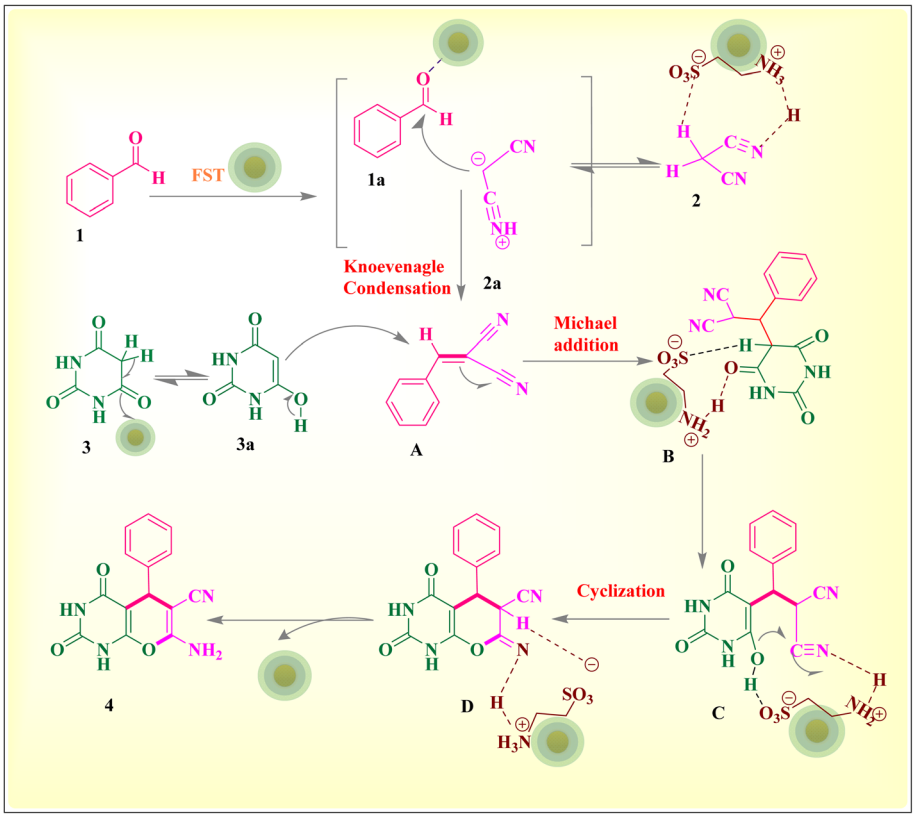

Scheme 3 Plausible mechanism.

derived carbanion. As a result, the formation of the arylidene malononitrile intermediate occurs more rapidly. Moreover, the nucleophilic addition to this intermediate is also accelerated.

4 Conclusion

In summary, we have successfully synthesized and characterized a magnetically recoverable Fe_3O_4@SiO_2@taurine nanocatalyst and demonstrated its excellent catalytic activity in the one-pot, three-component synthesis of pyrano[2,3-*d*]pyrimidine derivatives. Comprehensive analyses (FT-IR, XRD, TEM, SEM-EDS, TGA, Zeta and BET) confirmed the structural integrity, thermal stability, and effective surface functionalization of the nanocomposite. The catalyst exhibited high efficiency, affording excellent yields in short reaction times under green solvent conditions, while also offering easy magnetic separation and reusability over multiple cycles with negligible loss of activity. Compared to conventional catalysts, Fe_3O_4@SiO_2@taurine provides a sustainable, non-toxic, and cost-effective alternative for heterocyclic synthesis. These results highlight its potential as a versatile platform for green organic transformations, paving the way for broader applications in sustainable catalysis and pharmaceutical chemistry.

Conflicts of interest

The authors declare no conflict of interest, financial or otherwise.

Data availability

All data supporting the findings of this study are included within the article. This comprises detailed experimental procedures and all characterization and analytical data (FTIR, XRD, SEM, TEM, VSM and NMR spectra). No additional datasets were generated or analysed during the current study.

Acknowledgements

The authors are highly thankful to the Ministry of Education and SPD-RUSA Rajasthan for the support received under the RUSA-2.0 Project (F30(16)SPD/RUSA/2026/178). We sincerely thank the Department of Chemistry, Mohanlal Sukhadia University (MLSU), for providing NMR spectral facilities, and greatly appreciate the MNIT Jaipur facilities for timely assistance with FTIR, XRD, HR-TEM, and FESEM analyses. We thank SAIF/CIL Punjab University for providing BET and zeta potential analysis. We also acknowledge the Central University of Gujarat for providing the TGA facility. CA gratefully acknowledges the ANRF-PAIR-B grant (ANRF/PAIR/2025/000015/PAIR-B).

References

1 V. Polshettiwar and R. S. Varma, Green Chemistry by Nano-Catalysis, *Green Chem.*, 2010, **12**(5), 743, DOI: 10.1039/b921171c.

2 Z. Varzi and A. Maleki, Design and Preparation of ZnS-$ZnFe_2O_4$: A Green and Efficient Hybrid Nanocatalyst for the Multicomponent Synthesis of 2,4,5-triaryl-1 *H* -imidazoles, *Appl. Organomet. Chem.*, 2019, **33**(8), e5008, DOI: 10.1002/aoc.5008.

3 D. K. Jambhulkar, R. P. Ugwekar, B. A. Bhanvase and D. P. Barai, A Review on Solid Base Heterogeneous Catalysts: Preparation, Characterization and Applications, *Chem. Eng. Commun.*, 2022, **209**(4), 433–484, DOI: 10.1080/00986445.2020.1864623.

4 S. B. Kalidindi and B. R. Jagirdar, Nanocatalysis and Prospects of Green Chemistry, *ChemSusChem*, 2012, **5**(1), 65–75, DOI: 10.1002/cssc.201100377.

5 M. Duan, L. Jiang, G. Zeng, D. Wang, W. Tang, J. Liang, H. Wang, D. He, Z. Liu and L. Tang, Bimetallic Nanoparticles/Metal-Organic Frameworks: Synthesis, Applications and Challenges, *Appl. Mater. Today*, 2020, **19**, 100564, DOI: 10.1016/j.apmt.2020.100564.

6 S. Vásquez-Céspedes, R. C. Betori, M. A. Cismesia, J. K. Kirsch and Q. Yang, Heterogeneous Catalysis for Cross-Coupling Reactions: An Underutilized Powerful and Sustainable Tool in the Fine Chemical Industry?, *Org. Process Res. Dev.*, 2021, **25**(4), 740–753, DOI: 10.1021/acs.oprd.1c00041.

7 M. Shokouhimehr, K. Hong, T. H. Lee, C. W. Moon, S. P. Hong, K. Zhang, J. M. Suh, K. S. Choi, R. S. Varma and H. W. Jang, Magnetically Retrievable Nanocomposite Adorned with Pd Nanocatalysts: Efficient Reduction of Nitroaromatics in Aqueous Media, *Green Chem.*, 2018, **20**(16), 3809–3817, DOI: 10.1039/C8GC01240G.

8 S. Azad and B. B. F. Mirjalili, One-Pot Solvent-Free Synthesis of 2,3-Dihydro-2-Substituted-1H-Naphtho[1,2-e][1,3]Oxazine Derivatives Using Fe3O4@nano-Cellulose/TiCl as a Bio-Based and Recyclable Magnetic Nano-Catalyst, *Mol. Divers.*, 2019, **23**(2), 413–420, DOI: 10.1007/s11030-018-9884-6.

9 N. Kerru, S. V. H. S. Bhaskaruni, L. Gummidi, S. N. Maddila, P. Singh and S. B. Jonnalagadda, Efficient Synthesis of Novel Pyrazole-Linked 1,2,4-Triazolidine-3-Thiones Using Bismuth on Zirconium Oxide as a Recyclable Catalyst in Aqueous Medium, *Mol. Divers.*, 2020, **24**(2), 345–354, DOI: 10.1007/s11030-019-09957-0.

10 S. F. Hamzavi, S. Gerivani, S. Saeedi, K. Naghdipari and G. Shahverdizadeh, Preparation and Characterization of a Novel Spherical Cellulose–Copper(II) Oxide Composite Particles: As a Heterogeneous Catalyst for the Click Reaction, *Mol. Divers.*, 2020, **24**(1), 201–209, DOI: 10.1007/s11030-019-09942-7.

11 R. S. Varma, Greener and Sustainable Trends in Synthesis of Organics and Nanomaterials, *ACS Sustain. Chem. Eng.*, 2016, **4**(11), 5866–5878, DOI: 10.1021/acssuschemeng.6b01623.

12 H. Kiyani and F. Ghorbani, Efficient Tandem Synthesis of a Variety of Pyran-Annulated Heterocycles, 3,4-Disubstituted Isoxazol-5(4H)-Ones, and α,β-Unsaturated Nitriles Catalyzed by Potassium Hydrogen Phthalate in Water, *Res. Chem. Intermed.*, 2015, **41**(10), 7847–7882, DOI: 10.1007/s11164-014-1863-7.

13 H. Ostadzadeh and H. Kiyani, Multicomponent Synthesis of Tetrahydrobenzo[*b*]Pyrans, Pyrano[2,3- *d*]Pyrimidines, and Dihydropyrano[3,2- *c*]Chromenes Catalyzed by Sodium Benzoate, *Polycycl. Aromat. Compd.*, 2023, **43**(10), 9318–9337, DOI: 10.1080/10406638.2022.2162091.

14 Z. Faramarzi and H. Kiyani, Steglich's Base Catalyzed Three-Component Synthesis of Isoxazol-5-Ones, *Polycycl. Aromat. Compd.*, 2023, **43**(4), 3099–3121, DOI: 10.1080/10406638.2022.2061533.

15 S. Kamalifar and H. Kiyani, Facile and Efficient Synthesis of 9-Aryl-1,8-Dioxo-Octahydroxanthenes Catalyzed by Sulfacetamide, *Polycycl. Aromat. Compd.*, 2022, **42**(6), 3675–3693, DOI: 10.1080/10406638.2021.1872656.

16 Y. Chan, J. P. Zimmer, M. Stroh, J. S. Steckel, R. K. Jain and M. G. Bawendi, Incorporation of Luminescent Nanocrystals into Monodisperse Core–Shell Silica Microspheres, *Adv. Mater.*, 2004, **16**(23–24), 2092–2097, DOI: 10.1002/adma.200400237.

17 Y. H. Deng, W. L. Yang, C. C. Wang and S. K. Fu, A Novel Approach for Preparation of Thermoresponsive Polymer Magnetic Microspheres with Core–Shell Structure, *Adv. Mater.*, 2003, **15**(20), 1729–1732, DOI: 10.1002/adma.200305459.

18 Y. Lu, Y. Yin, B. T. Mayers and Y. Xia, Modifying the Surface Properties of Superparamagnetic Iron Oxide Nanoparticles through A Sol−Gel Approach, *Nano Lett.*, 2002, **2**(3), 183–186, DOI: 10.1021/nl015681q.

19 D. Yang, J. Hu and S. Fu, Controlled Synthesis of Magnetite−Silica Nanocomposites *via* a Seeded Sol−Gel Approach, *J. Phys. Chem. C*, 2009, **113**(18), 7646–7651, DOI: 10.1021/jp900868d.

20 X. Xu, C. Deng, M. Gao, W. Yu, P. Yang and X. Zhang, Synthesis of Magnetic Microspheres with Immobilized Metal Ions for Enrichment and Direct Determination of Phosphopeptides by Matrix-Assisted Laser Desorption Ionization Mass Spectrometry, *Adv. Mater.*, 2006, **18**(24), 3289–3293, DOI: 10.1002/adma.200601546.

21 Y. Deng, D. Qi, C. Deng, X. Zhang and D. Zhao, Superparamagnetic High-Magnetization Microspheres with an Fe_3O_4 @SiO_2 Core and Perpendicularly Aligned Mesoporous SiO_2 Shell for Removal of Microcystins, *J. Am. Chem. Soc.*, 2008, **130**(1), 28–29, DOI: 10.1021/ja0777584.

22 J. Ge, Q. Zhang, T. Zhang and Y. Yin, Core–Satellite Nanocomposite Catalysts Protected by a Porous Silica Shell: Controllable Reactivity, High Stability, and Magnetic Recyclability, *Angew. Chem.*, 2008, **120**(46), 9056–9060, DOI: 10.1002/ange.200803968.

23 S. Chen, J. Feng, X. Guo, J. Hong and W. Ding, One-Step Wet Chemistry for Preparation of Magnetite Nanorods, *Mater. Lett.*, 2005, **59**(8–9), 985–988, DOI: 10.1016/j.matlet.2004.11.043.

24 T. K. Kim, M. N. Lee, S. H. Lee, Y. C. Park, C. K. Jung and J.-H. Boo, Development of Surface Coating Technology of TiO2 Powder and Improvement of Photocatalytic Activity by Surface Modification, *Thin Solid Films*, 2005, **475**(1–2), 171–177, DOI: 10.1016/j.tsf.2004.07.021.

25 H. Zou, Z. Luo, X. Yang, Q. Xie and Y. Zhou, Toward Emerging Applications Using Core–Shell Nanostructured Materials: A Review, *J. Mater. Sci.*, 2022, **57**(24), 10912–10942, DOI: 10.1007/s10853-022-07328-z.

26 Y. Zhao, Co-Precipitated Ni/Mn Shell Coated Nano Cu-Rich Core Structure: A Phase-Field Study, *J. Mater. Res. Technol.*, 2022, **21**, 546–560, DOI: 10.1016/j.jmrt.2022.09.032.

27 M. Rimoldi, A. J. Howarth, M. R. DeStefano, L. Lin, S. Goswami, P. Li, J. T. Hupp and O. K. Farha, Catalytic Zirconium/Hafnium-Based Metal–Organic Frameworks, *ACS Catal.*, 2017, **7**(2), 997–1014, DOI: 10.1021/acscatal.6b02923.

28 T. L. H. Doan, T. Q. Dao, H. N. Tran, P. H. Tran and T. N. Le, An Efficient Combination of Zr-MOF and Microwave Irradiation in Catalytic Lewis Acid Friedel–Crafts Benzoylation, *Dalton Trans.*, 2016, **45**(18), 7875–7880, DOI: 10.1039/C6DT00827E.

29 V. T. Nguyen, H. Q. Ngo, D. T. Le, T. Truong and N. T. S. Phan, Iron-Catalyzed Domino Sequences: One-Pot Oxidative Synthesis of Quinazolinones Using Metal–Organic Framework Fe 3 O(BPDC) 3 as an Efficient Heterogeneous Catalyst, *Chem. Eng. J.*, 2016, **284**, 778–785, DOI: 10.1016/j.cej.2015.09.036.

30 S. Klotz, G. Steinle-Neumann, Th. Strässle, J. Philippe, Th. Hansen and M. J. Wenzel, Magnetism and the Verwey Transition in Fe 3 O 4 under Pressure, *Phys. Rev. B:Condens. Matter Mater. Phys.*, 2008, **77**(1), 012411, DOI: 10.1103/PhysRevB.77.012411.

31 M. Bonini, A. Wiedenmann and P. Baglioni, Synthesis and Characterization of Magnetic Nanoparticles Coated with a Uniform Silica Shell, *Mater. Sci. Eng. C*, 2006, **26**(5–7), 745–750, DOI: 10.1016/j.msec.2005.09.042.

32 R. Dawn, M. Zzaman, F. Faizal, C. Kiran, A. Kumari, R. Shahid, C. Panatarani, I. M. Joni, V. K. Verma, S. K. Sahoo, K. Amemiya and V. R. Singh, Origin of Magnetization in Silica-Coated Fe3O4 Nanoparticles Revealed by Soft X-Ray Magnetic Circular Dichroism, *Braz. J. Phys.*, 2022, **52**(3), 99, DOI: 10.1007/s13538-022-01102-x.

33 M. H. R. Farimani, N. Shahtahmasebi, M. Rezaee Roknabadi, N. Ghows and A. Kazemi, Study of Structural and Magnetic Properties of Superparamagnetic Fe3O4/SiO2 Core–Shell Nanocomposites Synthesized with Hydrophilic Citrate-Modified Fe3O4 Seeds *via* a Sol–Gel Approach, *Phys. E*, 2013, **53**, 207–216, DOI: 10.1016/j.physe.2013.04.032.

34 S. Sobhanardakani, A. Jafari, R. Zandipak and A. Meidanchi, Removal of Heavy Metal (Hg(II) and Cr(VI)) Ions from Aqueous Solutions Using Fe2O3@SiO2 Thin Films as a Novel Adsorbent, *Process Saf. Environ. Prot.*, 2018, **120**, 348–357, DOI: 10.1016/j.psep.2018.10.002.

35 N. Daneshvar, F. Shirini, M. S. N. Langarudi and R. Karimi-Chayjani, Taurine as a Green Bio-Organic Catalyst for the Preparation of Bio-Active Barbituric and Thiobarbituric Acid Derivatives in Water Media, *Bioorganic Chem*, 2018, **77**, 68–73, DOI: 10.1016/j.bioorg.2017.12.021.

36 F. Shirini and N. Daneshvar, Introduction of Taurine (2-Aminoethanesulfonic Acid) as a Green Bio-Organic Catalyst for the Promotion of Organic Reactions under Green Conditions, *RSC Adv.*, 2016, **6**(111), 110190–110205, DOI: 10.1039/C6RA15432H.

37 F. Ahangaran, A. Hassanzadeh and S. Nouri, Surface Modification of Fe3O4@SiO2 Microsphere by Silane Coupling Agent, *Int. Nano Lett.*, 2013, **3**(1), 23, DOI: 10.1186/2228-5326-3-23.

38 M. Fuentes-Pérez, M. Sotelo-Lerma, J. L. Fuentes-Ríos, E. G. Morales-Espinoza, M. Serrano and M. E. Nicho, Synthesis and Study of Physicochemical Properties of Fe3O4@ZnFe2O4 Core/Shell Nanoparticles, *J. Mater. Sci. Mater. Electron.*, 2021, **32**(12), 16786–16799, DOI: 10.1007/s10854-021-06236-3.

39 S. Sharifi Sharifabad, B. B. F. Mirjalili and A. Bamoniri, Nano-SiO2/Taurine as a New Natural Based Catalyst for Synthesis of Hexahydroquinolines Derivative, *Iran. J. Catal.*, 2022, **12**(3), 365–372, DOI: 10.30495/ijc.2022.1959104.1936.

40 S. S. Alterary and A. AlKhamees, Synthesis, Surface Modification, and Characterization of Fe_3 O_4 @SiO_2 Core@shell Nanostructure, *Green Process. Synth.*, 2021, **10**(1), 384–391, DOI: 10.1515/gps-2021-0031.

41 I. Devi, B. S. D. Kumar and P. J. Bhuyan, A Novel Three-Component One-Pot Synthesis of Pyrano[2,3-d]Pyrimidines and Pyrido[2,3-d]Pyrimidines Using Microwave Heating in the Solid State, *Tetrahedron Lett.*, 2003, **44**(45), 8307–8310, DOI: 10.1016/j.tetlet.2003.09.063.

42 S. Balalaie, S. Abdolmohammadi, H. R. Bijanzadeh and A. M. Amani, Diammonium Hydrogen Phosphate as a Versatile and Efficient Catalyst for the One-Pot Synthesis of Pyrano[2,3-d]Pyrimidinone Derivatives in Aqueous Media, *Mol. Divers.*, 2008, **12**(2), 85–91, DOI: 10.1007/s11030-008-9079-7.

43 M. Bararjanian, S. Balalaie, B. Movassag and A. M. Amani, One-Pot Synthesis of Pyrano[2,3-d]Pyrimidinone Derivatives Catalyzed by L-Proline in Aqueous Media, *J. Iran. Chem. Soc.*, 2009, **6**(2), 436–442, DOI: 10.1007/BF03245854.

44 A. Mobinikhaledi, N. Foroughifar and M. A. Bodaghi Fard, Eco-Friendly and Efficient Synthesis of Pyrano[2,3- *d*] Pyrimidinone and Tetrahydrobenzo[*b*]Pyran Derivatives in Water, *Synth. React. Inorg. Met.-Org. Nano-Met. Chem.*, 2010, **40**(3), 179–185, DOI: 10.1080/15533171003629121.

45 H. Nagabhushana, S. Sandeep Saundalkar, L. Muralidhar, B. M. Nagabhushana, C. R. Girija, D. Nagaraja, M. A. Pasha and V. P. Jayashankara, α-Fe2O3 Nanoparticles: An Efficient, Inexpensive Catalyst for the One-Pot Preparation of 3,4-Dihydropyrano[c]Chromenes, *Chin. Chem. Lett.*, 2011, **22**(2), 143–146, DOI: 10.1016/j.cclet.2010.09.020.

46 M. M. Heravi, A. Ghods, K. Bakhtiari and F. Derikvand, Zn [(L)Proline]$_2$: An Efficient Catalyst for the Synthesis of Biologically Active Pyrano[2,3- *d*]Pyrimidine Derivatives, *Synth. Commun.*, 2010, **40**(13), 1927–1931, DOI: 10.1080/00397910903174390.

47 G. M. Ziarani, S. Faramarzi, S. Asadi, A. Badiei, R. Bazl and M. Amanlou, Three-Component Synthesis of Pyrano[2,3-d]-Pyrimidine Dione Derivatives Facilitated by Sulfonic Acid Nanoporous Silica (SBA-Pr-SO3H) and Their Docking and

Urease Inhibitory Activity, *DARU J. Pharm. Sci.*, 2013, **21**(1), 3, DOI: 10.1186/2008-2231-21-3.

48 R. Ramesh and A. Lalitha, Synthesis of Pyran Annulated Heterocyclic Scaffolds: A Highly Convenient Protocol Using Dimethylamine, *Res. Chem. Intermed.*, 2015, **41**(10), 8009–8017, DOI: 10.1007/s11164-014-1873-5.

49 R. Karimi-Chayjani, N. Daneshvar, H. Tajik and F. Shirini, Introduction of a New Magnetic Nanocatalyst as an Organic-inorganic Hybrid Framework for the Synthesis of Pyrano[2,3- *d*]Pyrimidinone(Thione)s and Pyrido[2,3- *d*] Pyrimidines, *ChemistrySelect*, 2019, **4**(4), 1205–1213, DOI: 10.1002/slct.201802916.

50 S. Sajjadifar and Z. Gheisarzadeh, Isatin-SO_3 H Coated on Amino Propyl Modified Magnetic Nanoparticles (Fe_3 O_4 @APTES@isatin-SO_3 H) as a Recyclable Magnetic Nanoparticle for the Simple and Rapid Synthesis of Pyrano [2,3-d] Pyrimidines Derivatives, *Appl. Organomet. Chem.*, 2019, **33**(1), e4602, DOI: 10.1002/aoc.4602.

51 F. Mohamadpour, Supramolecular β-Cyclodextrin as a Biodegradable and Reusable Catalyst Promoted Environmentally Friendly Synthesis of Pyrano[2,3- *d*] Pyrimidine Scaffolds *via* Tandem Knoevenagel–Michael–Cyclocondensation Reaction in Aqueous Media, *Polycycl. Aromat. Compd.*, 2022, **42**(5), 2805–2814, DOI: 10.1080/10406638.2020.1852274.

52 S. Sorkhabi, R. Mozafari and M. Ghadermazi, New Advances in Catalytic Performance of Erbium-folic Acid-coated $CoFe_2$ O_4 Complexes for Green One-pot Three-component Synthesis of Pyrano[2,3- *d*]Pyrimidinone and Dihydropyrano[3,2- *c*]Chromenes Compounds in Water, *Appl. Organomet. Chem.*, 2021, **35**(7), e6225, DOI: 10.1002/aoc.6225.

53 M. Nikpassand, L. Z. Fekri, R. S. Varma, L. Hassanzadi and F. S. Pashaki, Green Synthesis of Novel 5-Amino-Bispyrazole-4-Carbonitriles Using a Recyclable Fe_3 O_4 @SiO_2 @vanillin@thioglycolic Acid Nano-Catalyst, *RSC Adv.*, 2022, **12**(2), 834–844, DOI: 10.1039/D1RA08001F.

54 H. N. Akolkar, S. G. Dengale, K. K. Deshmukh, B. K. Karale, N. R. Darekar, V. M. Khedkar and M. H. Shaikh, Design, Synthesis and Biological Evaluation of Novel Furan & Thiophene Containing Pyrazolyl Pyrazolines as Antimalarial Agents, *Polycycl. Aromat. Compd.*, 2022, **42**(5), 1959–1971, DOI: 10.1080/10406638.2020.1821231.

55 F. Ghorbani, H. Kiyani and S. A. Pourmousavi, Facile and Expedient Synthesis of α,β-Unsaturated Isoxazol-5(4H)-Ones under Mild Conditions, *Res. Chem. Intermed.*, 2020, **46**(1), 943–959, DOI: 10.1007/s11164-019-03999-7.

56 S. Aslanpour and H. Kiyani, Rapid Synthesis of Fully Substituted Arylideneisoxazol-5(4H)-One Using Zinc Oxide Nanoparticles, *Res. Chem. Intermed.*, 2023, **49**(10), 4603–4619, DOI: 10.1007/s11164-023-05059-7.

57 A. Azimi-Roshan, H. Kiyani and M. Mamaghani, Green Pseudo-Seven Component Synthesis of Tris-Cyclohexylamino-Oxo-Benzene- 1,3,5-Tricarboxylates *via* Passerini Reaction under Aqueous Conditions, *Curr. Org. Chem.*, 2025, **29**(13), 1057–1065, DOI: 10.2174/0113852728269992241030054239.